

INORGANIC
CHEMISTRY
FRONTIERS



From Unprecedented 2,2□-Bisimidazole-Bridged Rare Earth Organometallics to Magnetic Hysteresis in the Dysprosium congener

Journal:	<i>Inorganic Chemistry Frontiers</i>
Manuscript ID	QI-RES-03-2023-000546.R1
Article Type:	Research Article
Date Submitted by the Author:	05-May-2023
Complete List of Authors:	Benner, Florian; Michigan State University, Chemistry Demir, Selvan; Michigan State University, Chemistry

SCHOLARONE™
Manuscripts

ARTICLE

From Unprecedented 2,2'-Bisimidazole-Bridged Rare Earth Organometallics to Magnetic Hysteresis in the Dysprosium Congener

Received 00th January 20xx,
Accepted 00th January 20xx

DOI: 10.1039/x0xx00000x

Florian Benner, and Selvan Demir*

The first use of the bare 2,2'-bisimidazole (H_2bim) ligand in rare earth metal chemistry is presented. The series of symmetric dinuclear complexes $[(Cp^*RE)_2(\mu-bim)]$ were synthesized from the salt metathesis reaction of the lithium salt $Li_2(bim)$ with $Cp^*RE(BPh_4)$ ($RE = Y$ (**1**), Gd (**2**), Dy (**3**); $Cp^* = 1,2,3,4,5$ -pentamethylcyclopentadienyl). The isostructural complexes **1-3** were unambiguously characterized through elemental analysis, NMR, IR and UV/Vis spectroscopy, single-crystal X-ray diffraction, SQUID magnetometry and density functional theory (DFT) calculations. Intriguingly, the compounds are redox-inactive both on the timescale of chemical and electrochemical experiments. Herein, a rationale for the redox innocence of the bim^{2-} ligand is provided by calculations of the electron affinity and ionization potential, both correlating well with topologically similar structures of comparable complexes. Remarkably, the Dy complex **3** shows open magnetic hysteresis loops up to 5 K which is rare for lanthanide SMMs with bridging diamagnetic entities. AC magnetic susceptibility measurements at zero field revealed slow magnetic relaxation up to 26 K leading to an effective energy barrier to spin reversal of $U_{eff} = 154(2) \text{ cm}^{-1}$ and $\tau_0 = 5(1) \times 10^{-8} \text{ s}$. The lanthanides are weakly, antiferromagnetically coupled, where the J value for the Gd -congener **2** was determined to be $-0.074(2) \text{ cm}^{-1}$.

Introduction

The rational design of polynuclear molecular lanthanide (Ln) complexes has sparked tremendous interest among chemists to uncover novel catalytic reactivity,¹ luminescence properties²⁻⁴ and single-molecule magnet (SMM) behavior. The latter requires the molecule's magnetic moment to exhibit a preferred orientation, giving rise to a bistable ground state, where spin "up" and "down" are separated by an energy barrier to spin reversal, U_{eff} . Since the first observation of slow magnetic relaxation in a molecule in the $[Mn_{12}O_{12}(CH_3COO)_{16}(H_2O)_4]$ complex in 1993,^{5,6} milestones in terms of SMM characteristics have been achieved by the use of highly anisotropic Ln^{III} ions such as Dy^{III} or Tb^{III} to form mononuclear⁷ and multinuclear complexes. The latter advance benefited from the implementation of radical bridges that are able to couple two lanthanide centers strongly together.⁸ Among those, owing to the short, highly charged bridge, dinitrogen radical-bridged systems are particularly impressive, where the organometallic terbium complex $[K(\text{crypt-222})][(Cp^{tet}Tb)_2(\mu-N_2^{3-\cdot})]$ (where $\text{crypt-222} = 2.2.2$ -cryptand; $Cp^{tet} = 1,2,3,4$ -tetramethylcyclopentadienyl) exhibits open hysteresis loops up to 30 K and maximum coercivity of 8 T, both the highest for a dinuclear compound containing a radical moiety.⁹ This is only surpassed by the mixed-valent dinuclear compound $(Cp^{Pr5})_2Dy_2$ which features record metrics for

SMMs in terms of spin-reversal barrier, blocking temperature, and coercivity.¹⁰ These advances are a testament of the enormous potential of coupling highly anisotropic lanthanide ions strongly together, and the number of such examples is small, thus, research towards this direction is desirable.¹¹⁻¹³

An underexplored ligand system is the tetraaza-analogue of fulvalene, 2,2'-bisimidazole (bim), which is composed of two bridged five-membered rings, each featuring two N atoms. Both the protonated (H_2bim) and deprotonated (bim^{2-}) have been used in coordination chemistry. Transition metal (TM) complexes feature the ligand in its protonated (H_2bim),¹⁴⁻²² ligands.

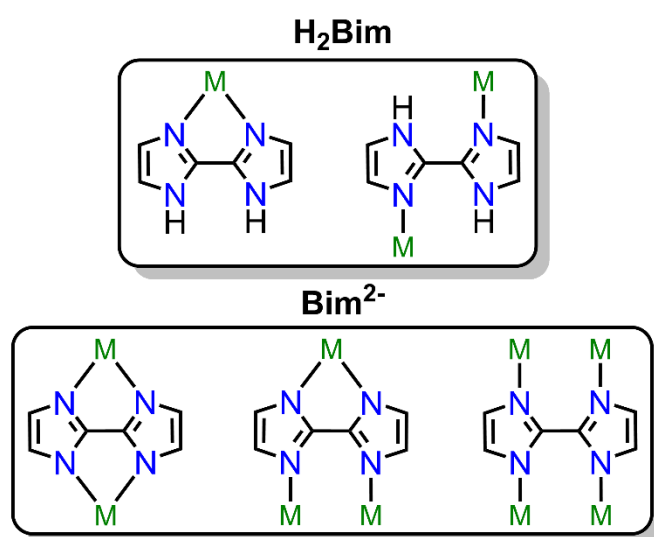


Chart 1. Excerpt of known coordination motives for H_2bim and bim^{2-} .

Department of Chemistry, Michigan State University, 578 South Shaw Lane, East Lansing, Michigan 48824, USA. E-mail: sdemir@chemistry.msu.edu

* Electronic supplementary information (ESI) available: 2251266 (1), 2251267 (2) and 2251271 (3). For ESI and crystallographic data in CIF or other electronic format see DOI: XXX

ARTICLE

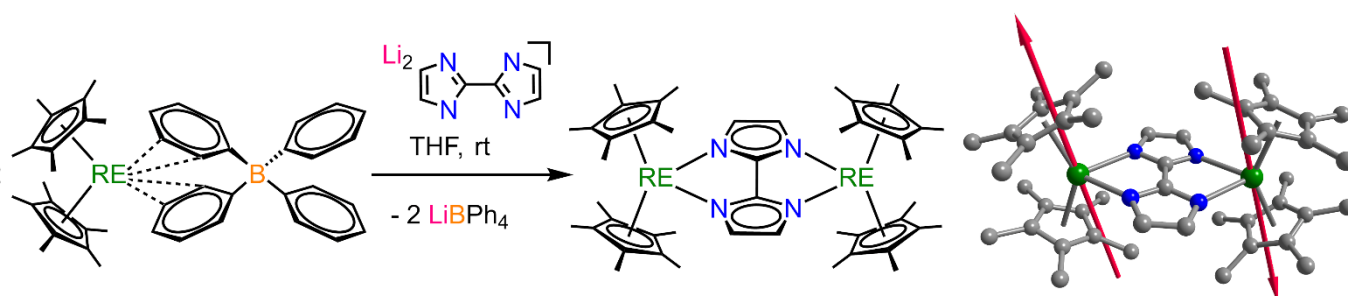


Figure 1. Synthesis of $[(\text{Cp}^*_2\text{RE})_2(\mu\text{-bim})]$ RE = Y (**1**), Gd (**2**), Dy (**3**), Li = $[\text{Li}(\text{PMDTA})]^+$ (left) via salt metathesis reaction of $\text{Cp}^*_2\text{RE}(\text{BPh}_4)$ and Li_2bim . Structure of **3** (right). Green, blue, and grey spheres represent dysprosium, nitrogen, and carbon atoms, respectively. All hydrogen atoms and lattice solvent molecules for **3** are omitted for clarity. Red arrows represent the orientation of the magnetic anisotropy of the $m_J = \pm 15/2$ state of Dy^{III} as calculated by Magellan.²³

Table 1. Selected interatomic distances (Å) and angles (deg) of the bim²⁻-bridged complexes, **1-3**.

	1	2	3
RE–N	2.412(3), 2.397(3)	2.424(3), 2.435(3)	2.417(2), 2.403(2)
Cnt ^a –RE	2.362, 2.369	2.405, 2.398	2.363, 2.374
C ₂ –C ₂ '	1.438(8)	1.452(7)	1.452(5)
M ^{III} –M	6.105(1)	6.169(1)	6.119(1)
Cnt ₁ –RE–Cnt ₂	137.1	137.8	137.6
RE–N–N–RE	13.5(5)	15.5(3)	15.2(3)

^aCnt = Centroid of the C₅Me₅ ligand.

singly deprotonated (Hbim⁻)^{19,24,25} or doubly deprotonated (bim²⁻)^{14,17,19,21,25–28} form. The degree of protonation affects the denticity of the ligand and provided access to mono-,^{14,16–21,25} di-,^{14,15,17,21,22,24–26,29–31} tri-,^{27,32} or tetranuclear complexes^{19,27,28} Chart 1. This structural richness gave rise to a wide range of applications where the TM complexes were luminescent,²² catalytically active,¹⁵ or intriguing for their spin-crossover properties.^{14,16} The various binding modes allowed also the construction of metal-organic frameworks^{28,31,32} or polyoxometallates.^{15,30} Furthermore, many complexes of H₂bim show strong ion pairing effects through hydrogen bonding of the N–H groups with anionic species,^{16,20} yielding exotic N–H-bridged dimeric complexes¹⁹ or potential applications in anion sensing.¹⁴

By comparison, H₂bim/bim²⁻ ligands are entirely unknown in molecular rare earth metal chemistry. In multidimensional systems, only four examples are known all of which are lanthanide (Ln) MOFs, where three of them contain N-carboxylate-substituted bim ligands^{33–35} and one features direct Ln–N-bonds to the bim.²⁹ This scarcity is surprising as its six-membered counterpart 2,2'-bipyrimidine (bpym) has found many promising applications in the fields of small-molecule activation^{36,37} and SMMs.³⁸

Here, we present the synthesis and characterization of the first bim-bridged rare earth (RE) complexes $(\text{Cp}^*_2\text{RE})_2\text{bim}$ (where Cp* = pentamethylcyclopentadienyl) with the RE metals yttrium (**1**), gadolinium (**2**), and dysprosium (**3**). The Cp*₂ ligand field was judiciously chosen due to its ability to reinforce the

preferred axial orientation of the Dy^{III} magnetic moment while providing sufficient steric hindrance to avoid equatorial coordination of solvent molecules.

Results and Discussion

The dinuclear bisimidazolone-bridged complexes were pursued via a salt metathesis strategy aiming at the synthesis of a pro-ligand and a metal source first which can readily exchange their counterions to produce a thermodynamically more stable side product. We employed the proligand $[(\text{Li}(\text{PMDTA}))_2\text{bim}]$ (PMDTA: 1,1,4,7,7-pentamethyldiethylenetriamine), where the Li cation is encapsulated in the tetradentate PMDTA chelate. This known lithium compound was prepared through deprotonation of commercially available H₂bim with ^tBuLi in the presence of the chelating PMDTA.²⁶ As a metal source, we used Cp*₂RE(BPh₄) (RE = Y, Gd, Dy),³⁸ each featuring a weakly coordinated BPh₄⁻ anionic ligand, which can easily be displaced via anionic ligands in salt elimination reactions.

The neutral complexes $[(\text{Cp}^*_2\text{RE})_2(\mu\text{-bim})]$ (RE = Y (**1**), Gd (**2**), Dy (**3**)) were generated through salt metathesis reactions of Cp*₂RE(BPh₄) (RE = Y, Gd, Dy) with $[(\text{Li}(\text{PMDTA}))_2\text{bim}]$ in THF at room temperature in 31% (**1**), 52% (**2**) and 52% (**3**) crystalline yields (Figure 1). Crystals suitable for X-ray diffraction analysis were obtained from cooling concentrated toluene solutions to –30 °C over the course of three days (Figure 1, Tables 1 and S1–S3). Compounds **1-3** crystallize in the monoclinic space group *P*2₁/*c* where each metal center is formally eight-coordinated by

ARTICLE

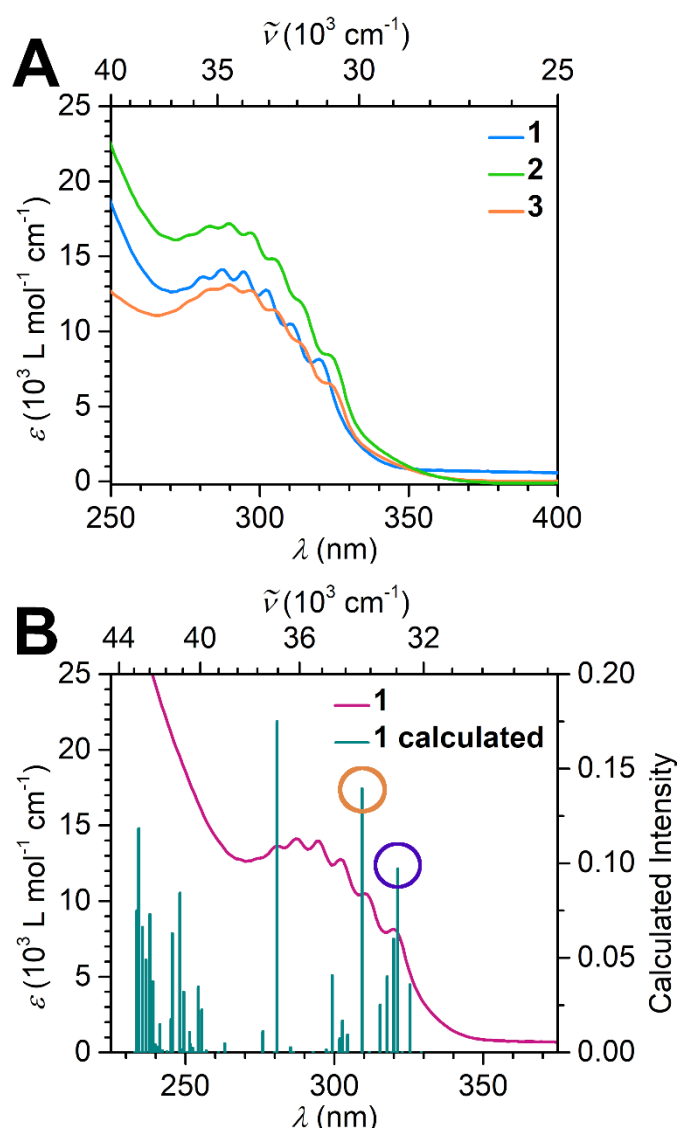


Figure 2. Magnified UV/Vis spectra of $[(\text{Cp}^*_2\text{RE})_2(\mu\text{-bim})]$ (blue line: Y (**1**); green line: Gd (**2**); orange line: Dy (**3**)) between 250 and 400 nm, taken in THF (A). Full spectra are shown in Figure S9. Overlay of experimental UV/Vis spectrum of **1** (purple line) with TDDFT-calculated transitions (green bars), B. Orange and purple circles highlight the transitions at 309 nm and 321 nm described in the text, which primarily involve bim-based transitions. Concentrations: 22.38 $\mu\text{mol/L}$ (**1**), 29.77 $\mu\text{mol/L}$ (**2**), 24.60 $\mu\text{mol/L}$ (**3**).

two Cp^* and two N atoms of a slightly asymmetrically coordinated bridging bim ligand with average RE–N distances 2.405(3) (**1**), 2.430 (**2**), 2.414(4) Å (**3**) comparable to the average 2.393(3) Å of the structurally related dysprosocenium complex $[\text{K}(\text{cryp-222})][(\text{Cp}^*_2\text{Ln})(\text{N},\text{N}'\text{-bpy}^{\text{B}})]$ bearing a dianionic 2,2'-bipyridine ligand (N,N'-bpy^B = 5,5'-bis(dimesitylboranyl)-2,2'-bipyridine).³⁹ Recently, we isolated the structurally closely related yttrium complex $[(\text{Cp}^*_2\text{Y})_2(\mu\text{-Bbim})]$ in which the bridge constitutes annulated bim, namely bisbenzimidazole (Bbim).⁴⁰ The

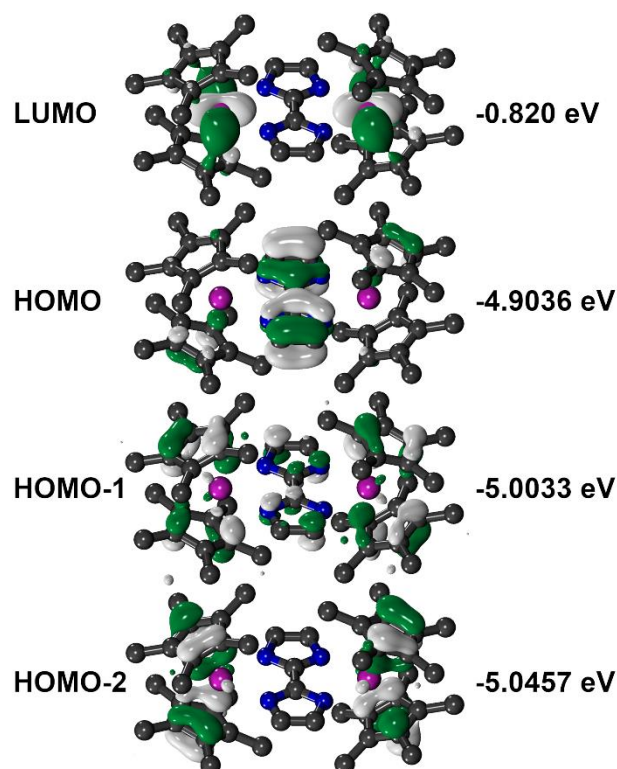


Figure 3. Graphical representation of calculated frontier orbitals partaking in the highlighted transitions (C). Orbital energies are given on the right in eV.

observed Cnt–RE–Cnt angles in **1-3** are slightly smaller (difference (Δ) = -1.5°) and the RE^{III}–RE–distances significantly shorter (Δ = -0.109 Å) than in the respective Bbim complex, indicative of a smaller steric repulsion between the two Cp^*_2RE scaffolds owing to the smaller bridging ligand. Moreover, the metal centers are symmetry-related through an inversion center residing on the bim $\text{C}_2\text{-C}_2'$ bond. In certain cases, the tetraphenylborate moiety within $\text{Cp}^*_2\text{RE}(\text{BPh}_4)$ is able to reduce redox-active ligands innate to accessible redox potentials such as phenazine (-1.83 V, vs. Fc/Fc^+),⁴¹ and thus, could potentially undergo a redox reaction with bim^{2-} to produce a radical bridge with a $3^{\cdot+}$ oxidation state, where the unpaired electron is localized in the ligands π^* -orbitals.⁴² However, the central $\text{C}_2\text{-C}_2'$ distance of 1.438(15) Å (**1**), 1.45(2) Å (**2**), and 1.448(4) Å (**3**), relative to 1.433(15) Å of the bim^{2-} -bridged diosmium complex $[\text{Os}^{\text{II}}(\text{bpy})_2]_2(\mu\text{-bim})(\text{ClO}_4)_2$,¹⁴ alluded to an unambiguous assignment of the bim oxidation state as -2 in **1-3**. Importantly, the radical oxidation state of $3^{\cdot+}$ for bim is hitherto unknown.

Owing to the very similar coordination sphere of around each metal center, a comparison of $[(\text{Cp}^*_2\text{Y})_2(\mu\text{-Bbim})]$ with **1** can aid to further understand structural trends arising from modifications of the bridging ligand. In spite of the presence of differing metal ions, in the first approximation the bonding situation is transferable to the dysprosium congener due to the

similar ionic radii (Y: 1.019 Å, Dy^{III}: 1.027 Å)⁴³ and electronic configuration 4d⁰5s⁰ (Y^{III}) and 4f⁹5d⁰6s⁰ (Dy^{III}), which leaves the Dy^{III} 4f valence shell strongly contracted and hindered for orbital overlap with ligand orbitals.

Despite the annulation of the bim moiety the ligand's electronic structure and bonding remain largely unaffected as proven by essentially identical C₂–C₂' bond distances of 1.438(8) Å (**1**), 1.452(7) Å (**2**), 1.448(4) Å (**3**) relative to 1.445(6) Å in [(Cp*₂Y)₂(μ-Bbim)].

The successful complexation of the bim²⁻ ligand can easily be traced by ¹H NMR spectroscopy on complex **1**, since the two diamagnetic Y^{III} ion facilitate execution and interpretation of nuclear magnetic resonance measurements, Figures S1-S3. In the ¹H-NMR spectrum of **1**, the presence of one aromatic singlet at 6.75 ppm and one aliphatic singlet at 1.87 ppm with an integral ratio of 4:60 can be associated with the bim²⁻ protons and Cp* methyl protons, respectively. In addition, paramagnetic ¹H NMR spectra of **2** and **3** were recorded at room temperature in C₆D₆ solutions. For **3**, a set of two broad signals at δ = -1.99 and -15.29 ppm occurs where the broadness is attributed to the presence of two paramagnetic Dy^{III} ions. The integration of these signals hints at a more pronounced shielding of the Cp* protons relative to the bim²⁻ proton resonances. For **2**, only one clearly paramagnetic signal at -25.1 ppm is observed, whereas the expected second signal might be obstructed by residual ⁿhexane. As observed for the other paramagnetic Ln ions before,^{44–46} the paramagnetic nature of Gd^{III} and Dy^{III} ions render ¹³C NMR experiments challenging. In fact, no ¹³C NMR signals were observed for complex **2** (compare Figure S4 to S5).

The complexation of the bim²⁻ ligand engenders also pronounced changes of the UV/Vis absorption spectra of **1–3** compared to reported spectra of the starting material Cp*₂Dy(BPh₄), Figures 3A and S9.⁴⁷ Most prominently, a broad band at ~300 nm emerged after complexation. This band stretches from 275 to 350 nm and is split into six discernible transitions at 281, 286, 294, 302, 311 and 320 nm for **1** and as such differs from the UV/Vis spectrum collected for [(Cp*₂Y)₂(μ-Bbim)], which features a broad transition between 275 and 395 nm with additional sharp transitions at 343 and 364 nm.⁴⁰ Hence, in both cases, the UV/Vis spectra must be strongly affected by transitions involving orbitals located on the bridging ligand, where the hypsochromic shift likely stems from a larger HOMO-LUMO gap in **1–3** owing to the absence of electron donating phenyl rings (Table S7).

TDDFT calculations on **1** were carried out to gain insight into the electronic excitation energies (Figure 3B and TableS4) using ORCA 5.0.3 (see SI for computational details).⁴⁸ The calculated, most intense transitions between 280 and 375 nm are excitations into the LUMO, which comprises a vacant Y centered *d*-orbital with negligible bim contributions (Figure 4). By contrast, the HOMO exhibits bim-based π-character with smaller Cp*–π contributions. The calculated most intense excitation into the LUMO at 281 nm constitutes to 83% of a low-lying Cp*–Y bonding orbital. The second most intense transition at 309 nm is composed of 39% of HOMO and 32% HOMO–1 excitations into the LUMO, representing π → (Y *d*)^{*} transitions. Similarly, the weaker 321 nm band constitutes a combination of

33% bonding (Cp*–Y) → π* and 37% π → (Y *d*)^{*} contributions. Direct HOMO → LUMO transitions also substantially contribute to the bands at 325 nm and 309 nm (35% and 39%, respectively), inducing ligand to metal charge transfer (LMCT) processes. Multiple weak excitations are predicted from the bim-centered HOMO and HOMO–1 into the HOMO+2 between 329 and 321 nm, corroborating with π → π* transitions.

For the sake of comparison, we also performed TDDFT calculations on [(Cp*₂Y)₂(μ-Bbim)] complex and contrasted the reported UV/Vis spectrum with the results in hand (Figures S10).⁴⁰ Similarly to **1**, the most intense transitions between 416 and 288 nm are the excitations into the LUMO, which is majorly a Bbim-based π*–orbital. At 416 nm, a transition from the Cp*–based HOMO into the LUMO is anticipated. A transition involving mostly Bbim-based orbitals is expected at 252 nm from HOMO–4 → HOMO+5, in accordance with a π → π* transition. This shows that the annulation of the bim moiety with two benzene rings in fact induces a significant blue shift of the π → π* transition by ~22%. By contrast, the HOMO→LUMO transition of **1** is blue-shifted by ~31% relative to the Bbim-bridged complex, which corresponds to an inhibited electron uptake in the smaller arene system.

The potential for ligand-based redox activity of **1** can be theoretically assessed by calculating the approximate adiabatic electron affinity *E*_{EA} and the ionization potential *E*_I via *E*_{EA} = *E*(**1**) – *E*(**1**⁻) and *E*_I = *E*(**1**⁺) – *E*(**1**), Table 2 and S7. The energies *E*(**1**⁻) and *E*(**1**⁺) represent the final energies of the hypothetical one-electron reduced and oxidized form of **1**, respectively.⁴⁹ These energies were obtained by performing unrestricted DFT geometry optimizations of the crystal coordinates of **1** with the respective charges and spin states set to +1/2 for **1**⁺, 0/1 for **1** and -1/2 for **1**⁻. The calculations provided values of *E*_{EA} = -0.2042 eV and *E*_I = 6.0225 eV, which imply that the chemical oxidation of **1** to a monoanionic bim^{-•} radical is exceedingly harder than the chemical reduction to a trianionic bim^{3-•} radical. Intriguingly, **1** was robust to all conducted chemical reduction experiments, even with the extremely strong reductant KC₈. Applying the same methodology, *E*_{EA} and *E*_I were also calculated for [(Cp*₂Y)₂(μ-Bbim)] innate to a diamagnetic Bbim²⁻ unit which, however, can be transformed to the trianionic bim^{3-•} radical when exposed to strong chemical reductants. This gives the unique opportunity to evaluate the effect of the additional fused phenyl rings on the oxidizability/reducibility of the central bisimidazole moiety. The shift of the energy level following the annulation of bisimidazole may be the key factor to enable chemical reduction of Bbim, namely through the narrower HOMO-LUMO gap and a diminished *E*_{EA}.

The calculations on [(Cp*₂Y)₂(μ-Bbim)] yielded *E*_{EA} of 0.6372 eV and *E*_I of 5.9663 eV and point to a similar trend to **1**, which is

Table 2. Calculated adiabatic electron affinities and ionization potentials for **1** and [(Cp*₂Y)₂(μ-Bbim)] on the uTPSSH/def2-SVP(Cp*)/def2-TZVP(Y,ligand)/D3BJ level of theory.

	<i>E</i> _I (eV)	<i>E</i> _{EA} (eV)
[(Cp* ₂ Y) ₂ (μ-bim)] (1)	6.0225	-0.2042
[(Cp* ₂ Y) ₂ (μ-Bbim)]	5.9663	0.6372

*E*_{EA}: electron affinity; *E*_I: ionization potential.

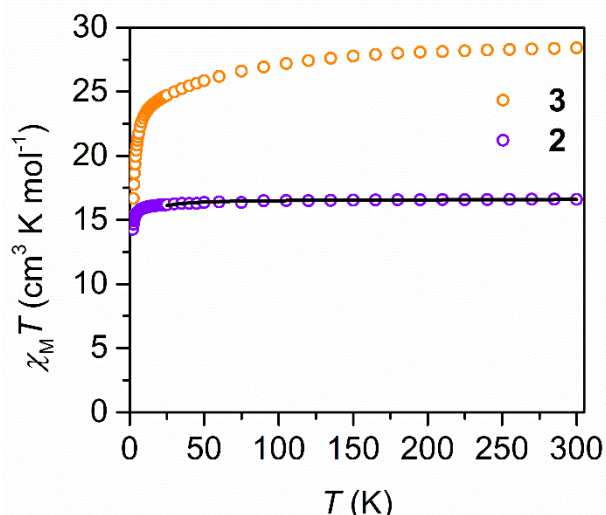


Figure 4. Variable-temperature dc magnetic susceptibility data for restrained polycrystalline samples of **2** (orange circles) and **3** (purple circles), collected under a 0.1 T applied dc field. The black line represents a fit to the data for **2** above 25 K giving rise to $g = 2.05414(6)$, $J = -0.074(2) \text{ cm}^{-1}$ and $zJ' = 0.0075 \text{ cm}^{-1}$.

that the chemical oxidation of Bbim^{2-} to a monoanionic Bbim^- radical is much harder than the chemical reduction to a trianionic bim^{3-} radical. This interpretation is in good agreement with our successful chemical reduction experiment to a bim^{3-} radical-bridged compound, while chemical oxidation attempts precluded access to a monoanionic radical-bridged complex. Notably, the calculated values obtained for **1** and $[(\text{Cp}^*_2\text{Y})_2(\mu\text{-Bbim})]$ are especially different with respect to the sign of

E_{EA} : **1** is negative E_{EA} and $(\text{Cp}^*_2\text{Y})_2\text{Bbim}$ is positive. A positive E_{EA} value signifies an electronically stable anionic state since energy is required to remove an electron. Whereas a negative E_{EA} value indicates an electronically metastable anion that can spontaneously eject an electron to regenerate the neutral species.^{50,51} Therefore, **1** is anticipated to be unstable upon chemical reduction, whereas the singly reduced $[(\text{Cp}^*_2\text{Y})_2(\mu\text{-Bbim})]^-$ complex is expected to be stable. In fact, this computational finding is consistent with the isolation of the Bbim radical-bridged complex $[\text{K}(\text{crypt-222})][(\text{Cp}^*_2\text{Y})_2(\mu\text{-Bbim}^{\cdot-})]$ containing a reduced bim^{3-} anion.⁴⁰

Lastly, the electrochemical properties of **1** and **3** were investigated via cyclic voltammetry to elucidate the redox activity of the bim^{2-} ligand captured between two metal ions (Figure S11). No redox activity was monitored through scanning towards negative potential, whereas scanning towards positive potentials revealed broad, irreversible oxidation events at applied potentials $>0.47 \text{ V}$ (vs Fc^+/Fc^0). These features substantially decreased in intensity upon repeated scanning cycles which may originate from irreversible chemical reactions of the analytes. The lack of any reversible features in all scans hints at the absence of an accessible, stable radical oxidation state for the bim ligand. Thus, the electrochemical results are in accord with the foregoing theoretical analysis and confirm the redox inactivity of the coordinated bim^{2-} ligand since the reduction is projected to be easier than the oxidation.

Static magnetic susceptibility behaviour

Direct current (dc) magnetic susceptibility data were collected on polycrystalline samples of **2** and **3** in applied magnetic fields of 0.1 T, 0.5 T and 1.0 T from 2 to 300 K (Figures 5, S12 and S13). The room temperature $\chi_{\text{M}}T$ value of $16.60 \text{ cm}^3 \text{ K mol}^{-1}$ for **2** at 0.1 T ($15.81 \text{ cm}^3 \text{ K mol}^{-1}$ at 1.0 T) is in accordance with the expected value of $15.75 \text{ cm}^3 \text{ K mol}^{-1}$ for two uncoupled Gd^{III} ions. Between 300 and 50 K, the $\chi_{\text{M}}T$ value remain almost unchanged and drop significantly at temperatures below 10 K, which is attributed to the thermal depopulation of low-lying excited states and/or antiferromagnetic coupling. Gd^{III} ions offer the unique opportunity to quantify the strength of magnetic exchange coupling because the orbital singlet is free of complications arising from spin-orbit coupling which typically occurs for ions such as Dy^{III} . Thus, the $\chi_{\text{M}}T$ vs. T data at 0.1 T for **2** was fit to a Heisenberg exchange Hamiltonian $\hat{H} = -2J_{\text{Gd-Gd}} \hat{S}_{\text{Gd}(1)} \hat{S}_{\text{Gd}(2)}$ where $J_{\text{Gd-Gd}}$ accounts for the exchange constant ascribed to the intramolecular $\text{Gd}^{\text{III}}\text{-Gd}^{\text{III}}$ coupling and $\hat{S}_{\text{Gd}(n)}$ is the spin operator for each Gd^{III} ion using Phi.⁵² A small antiferromagnetic intramolecular exchange coupling constant of $-0.074(2) \text{ cm}^{-1}$ with a small intermolecular coupling (zJ') of 0.0075 cm^{-1} was found for **2**. Notably, the inclusion of a zJ' contribution improved substantially the quality of the fit (see supporting information for details) alluding to the presence of a small antiferromagnetic intermolecular coupling with additional weak intramolecular ferromagnetic coupling. Such a small J value indicates weak coupling between the two metal ions which is typical for polynuclear Ln^{III} where the metal ions are bridged by diamagnetic ligands,^{53,54} since the lanthanides' valence $4f$ orbitals are extremely contracted preventing effective spin density transfer onto the bridging ligands. However, the exchange coupling can be greatly strengthened by implementing heavy p -block or radical ligands as bridges where their diffuse orbitals allow efficient suppression of undesirable quantum tunneling processes (QTM).⁵⁵⁻⁵⁹ An qualitative indication for strong magnetic coupling between the Ln^{III} ions would be rise in $\chi_{\text{M}}T$ at lower temperatures which is lacking in **2** and **3** further corroborating the weak coupling.

Unlike **2**, the $\chi_{\text{M}}T$ vs. T plot for **3** showed first a steady decline with decreasing temperature from 300 to 12 K, followed by a steep drop culminating at a value of $18.09 \text{ cm}^3 \text{ K mol}^{-1}$ at 2 K. The room temperature $\chi_{\text{M}}T$ value of $28.62 \text{ cm}^3 \text{ K mol}^{-1}$ at 0.1 T is in excellent agreement with the expected value of $28.33 \text{ cm}^3 \text{ K mol}^{-1}$ for two non-interacting Dy^{III} ions. The overall similar trend of the shape of the $\chi_{\text{M}}T$ vs. T plot of **3** relative to **2** points at similar weak coupling between the Dy^{III} ions.

Although the closest intermolecular $\text{Ln}\cdots\text{Ln}$ distances of $8.558(1) \text{ \AA}$ (**2**) and $8.538(1) \text{ \AA}$ (**3**) are rather long, close in-plane interactions are observed between the outer carbon atoms of the bim ligand and carbon atoms of the neighboring Cp^* ring ($3.478(5) \text{ \AA}$ (**2**)), hinting at a potential antiferromagnetic dipolar coupling pathway.

Dynamic magnetic susceptibility properties

Bisimidazolate ligands have never been employed in Ln -based single-molecule magnets (SMMs). Therefore, we were

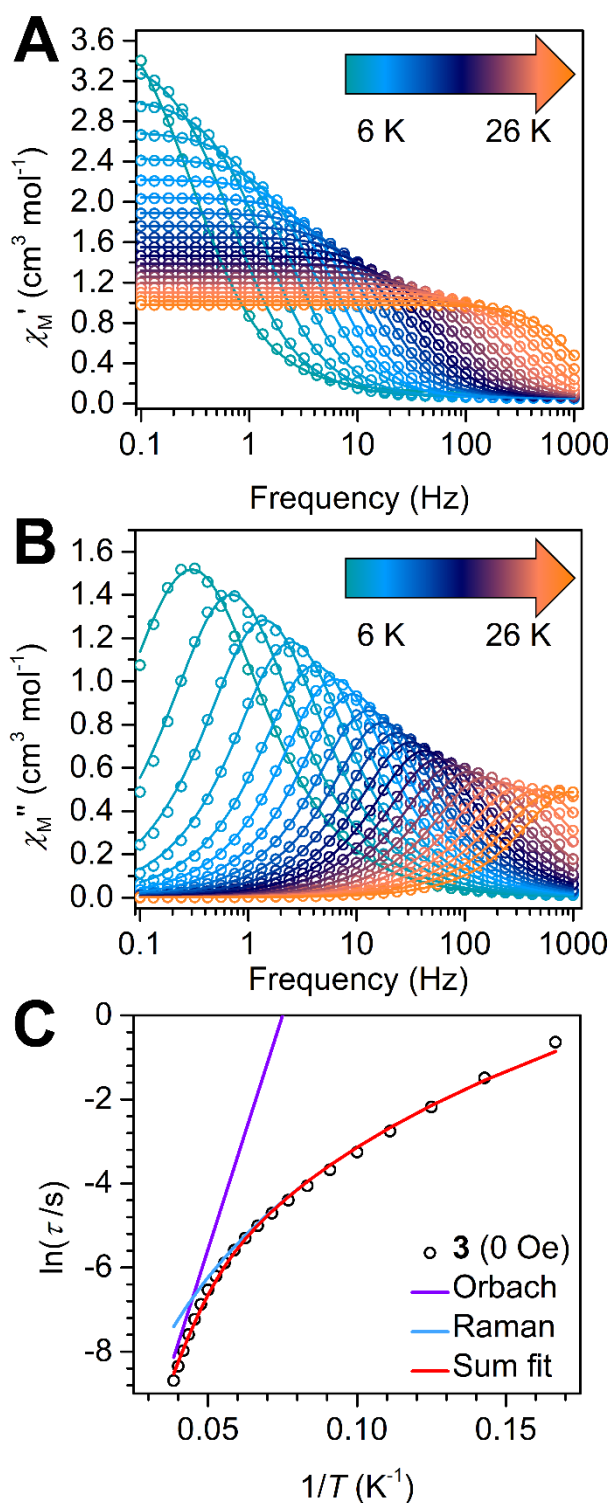


Figure 5. Variable-temperature, variable-frequency in-phase (χ_M') (A) and out-of-phase (χ_M'') (B) ac magnetic susceptibility data collected for **3** under a zero applied dc field from 2 to 26 K. Solid lines represent fits to the data between 6 and 26 K, as described in the main text. Arrhenius plot of relaxation time data derived from ac magnetic susceptibility measurements at temperatures from 6 to 26 K (black circles) for **3** (C). The red solid line represents a fit to an Orbach relaxation process and a Raman pathway. The best fit yielded $U_{\text{eff}} = 154(2) \text{ cm}^{-1}$ and $\tau_0 = 5(1) \times 10^{-8} \text{ s}$, $C = 7.9(2) \times 10^{-4} \text{ s}^{-1} \text{ K}^{-n}$, $n = 4.47(2)$. Green and violet solid lines represent Raman and Orbach contributions, respectively.

interested in exploring the interplay of exchange coupling between the anisotropic Ln^{III} ions and the local crystal field around each metal center. Although the intramolecular magnetic coupling is rather small, the magnetic moments of **3** may still relax slowly mostly owing to the local crystal field of the Dy^{III} ions as the single-ion magnetic anisotropy of each oblate-shaped Dy^{III} ion is generally exemplified when sandwiched in an axial coordination environment as in this case imposed by the two Cp* ligands. If additionally equatorial ligands around the lanthanide ion are avoided, then the anisotropy can be maximized as impressively demonstrated in mononuclear complexes.^{7,60,61} The most recent such example of the impact of a strongly axial ligand sphere is the retention of magnetic memory for 100 s at 66 K in a bisaminoborolide Dy^{III} complex.^{62,63}

To investigate the relaxation dynamics, variable-frequency variable-temperature in-phase (χ_M') and out-of-phase (χ_M'') ac magnetic susceptibility data were collected for a polycrystalline sample of **3** under a 3 Oe ac field at zero applied dc field, Figure 6. Here, the observation of χ_M'' signals imply the presence of an energy barrier to spin-reversal. Indeed, the Dy complex **3** exhibits temperature-dependent χ_M'' peak maxima between 2 and 26 K in the 0.1 and 1000 Hz frequency range which shift towards higher frequencies with rising temperatures. The collected ac magnetic susceptibility data were used to generate χ_M' vs. χ_M'' plots (Cole-Cole plots) at each temperature (Figure S14) and were then fitted by a generalized Debye model (program CCfit)⁶⁴ to extract the relaxation times, τ . The $\ln(\tau)$ vs. $1/T$ plots (Arrhenius plots) can be used to deconvolute the operating relaxation mechanisms by considering different temperature profiles (Figures 5C, S15 and S16). The temperature dependence of relaxation times provides insight into the operative relaxation processes at the given temperatures. An energy exchange of the system with the lattice via phonons to ascend to the cusp of the barrier corresponds to an activation barrier of spin relaxation which is referred to as Orbach process and is reflected by the exponential function $\tau^{-1} = \tau_0^{-1} \exp(-U_{\text{eff}}/k_B T)$, where U_{eff} is the energy barrier to spin reversal, τ_0 is the preexponential factor (or attempt time) and k_B is the Boltzmann constant. Temperature-independent relaxation times are commonly associated with quantum tunnelling of the magnetization and typically expressed as τ_{QTM}^{-1} . In addition, a relaxation process obeying a power law ($\tau^{-1} = CT^n$) is associated with the simultaneous absorption and emission of lattice phonons.

The best fit to the extracted τ values for **3** considered an Orbach and a Raman process giving rise to $U_{\text{eff}} = 154(2) \text{ cm}^{-1}$ and $\tau_0 = 5(1) \times 10^{-8} \text{ s}$, $C = 7.9(2) \times 10^{-4} \text{ s}^{-1} \text{ K}^{-n}$, $n = 4.47(2)$. The inclusion of a QTM contribution yielding $\tau_{\text{QTM}} = 10^{3.00(1)} \text{ s}$, had no impact on the Orbach and Raman parameters, hinting at a negligible through-barrier tunnelling process within the investigated temperature regime (Figure S16). By comparison, a linear fit to the relaxation times observed at the highest temperatures between 24 and 26 K gave an effective barrier to spin relaxation of $U_{\text{eff}} = 153.9(5) \text{ cm}^{-1}$ and a pre-exponential factor of $\tau_0 = 3.31(8) \times 10^{-8} \text{ s}$ (Figure S15). This attained barrier height from considering a pure Orbach process at high

temperatures matches perfectly with the U_{eff} value obtained for the full temperature range. Since the extraction of the τ data is limited by the frequency range measurable through a conventional ac magnetometer, the relaxation times below 6 K were not accessible through this method.

The application of a dc field during ac magnetic measurements can attenuate QTM by moving the corresponding $\pm m_J$ states out of resonance. The effect of dc fields of up to 3000 Oe on the relaxation behaviour of **3** was probed at 6 K, Figures 7 and S17. If the application of dc fields engenders a suppression of QTM, oftentimes a shift of the χ_M'' maxima towards lower frequencies occurs giving rise to longer τ times.⁶⁵ By contrast, subjecting **3** to increasing magnetic fields amplified the magnetic relaxation as indicated by the high-frequency shifts of the χ_M'' maxima, Figure S17. The plot of the extracted relaxation times versus dc fields exhibits first a gradual decline of τ with stronger dc fields passing through a minimum at 1150 Oe, followed by an ascent of τ to a local maximum at ~ 2000 Oe, and finally transitioning into a second descend, Figure 6. At 3000 Oe, the value for τ was diminished by 47% which suggests the onset of additional relaxation processes at higher fields, which is described as $\tau^{-1} = A H^4 T$. A direct process only occurs when the Zeeman splitting of a given state matches exactly a lattice phonon's energy and is therefore only observed under applied magnetic fields.⁶⁶ Variable-frequency, variable-temperature in-phase (χ_M') and out-of-phase (χ_M'') ac magnetic susceptibility data were collected for **3** at the optimum dc field of 2000 Oe, Figure 6B and S18. However, the obtained τ values were again best fit to a sum of Orbach and Raman processes, giving rise to $U_{\text{eff}} = 156(1) \text{ cm}^{-1}$ and $\tau_0 = 4.8(1) \times 10^{-8} \text{ s}$, $C = 1.5(2) \times 10^{-3} \text{ s}^{-1} \text{ K}^{-n}$, $n = 4.30(1)$, where U_{eff} is only marginally affected by the applied magnetic field, Figure S19. These findings emphasize the absence of a direct relaxation process within the field-range investigated here and rather a magnitude amplification of the Raman relaxation process through the dc field.

To explore the relaxation times below 6 K, we conducted dc magnetic relaxation experiments between 1.8 K and 4.0 K. In this technique a high magnetic field is applied to the sample to saturate the magnetization. The field is then quickly removed, which will cause the onset of magnetic relaxation that will follow an exponential decay. Hence, fitting these curves to an exponential function allows the extraction of τ at these low temperatures unattainable through ac techniques, Figures S20-S26. Fitting the combined Arrhenius plot of τ derived from ac and dc measurements versus inverse temperature was possible considering QTM, Raman and Orbach processes, Table S9 and Figure S27. The inclusion of all three relaxation processes allows for the phenomenological deconvolution of the relaxation processes as a function of temperature. At the lowest temperatures the relaxation times are temperature-dependent which is associated with quantum tunnelling of the magnetization. This is commonly observed for polynuclear Dy complexes featuring diamagnetic bridging ligands. A change between the temperature-independent QTM and power-law dependent Raman regime occurs around 3.2 K, where the relaxation times begin to be temperature-dependent. A second

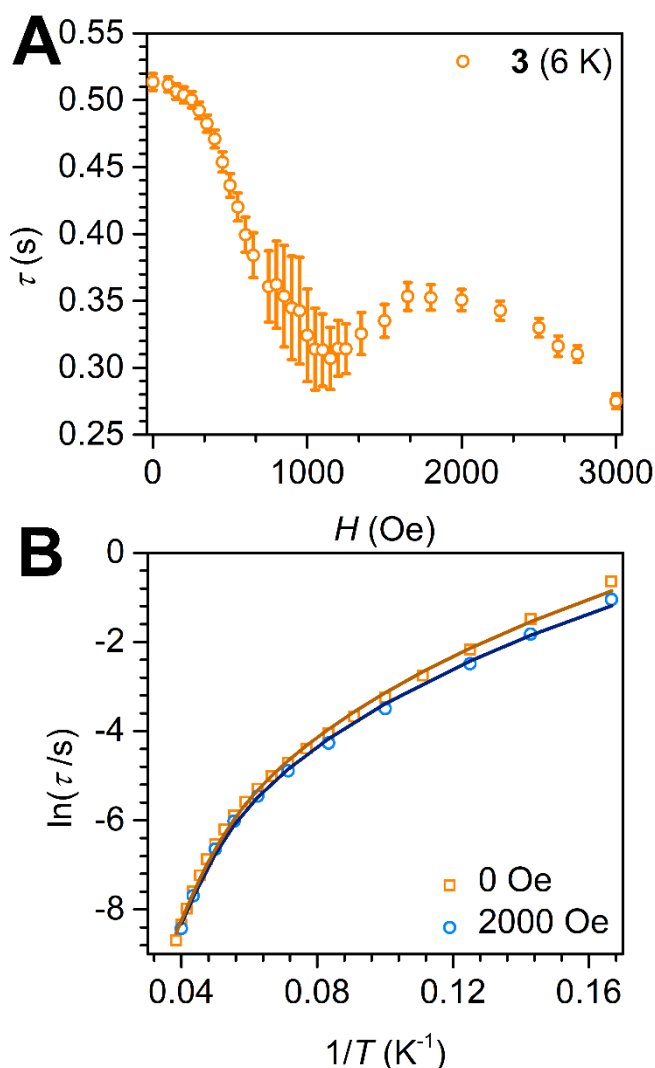


Figure 6. Variable-field, variable-frequency τ values for **3**, recorded at 6 K for dc fields up to 3000 Oe (A). Arrhenius plot of relaxation time data derived from ac magnetic susceptibility measurements at temperatures between 6 to 25 K under a 0 Oe (orange squares) and 2000 Oe applied DC field (blue circles) for **3** (B). The dark orange and blue solid lines represent fits to an Orbach relaxation process and a Raman pathway for the 0 Oe and 2000 Oe data, respectively. The best fit yielded $U_{\text{eff}} = 154(2) \text{ cm}^{-1}$ and $\tau_0 = 5(1) \times 10^{-8} \text{ s}$, $C = 7.9(2) \times 10^{-4} \text{ s}^{-1} \text{ K}^{-n}$, $n = 4.47(2)$ at 0 Oe and $U_{\text{eff}} = 156(1) \text{ cm}^{-1}$ and $\tau_0 = 4.8(1) \times 10^{-8} \text{ s}$, $C = 1.5(2) \times 10^{-3} \text{ s}^{-1} \text{ K}^{-n}$, $n = 4.30(1)$ at 2000 Oe. Green and violet solid lines represent Raman and Orbach contributions, respectively.

transition appears at around 16 K, where the Orbach process becomes dominant corresponding to a linear temperature dependence of the relaxation times.

Magnetization under variable fields

The final inspection of the efficacy of a single-molecule magnet behaviour represents the evaluation of the magnetic hysteresis behaviour, which is a key feature for information storage materials. This property is probed via field-dependent magnetization (M vs. H) experiments, which most prominently show either open hysteresis loops corresponding to a lack of QTM or waist-restricted curves, possibly with step-like features, hinting at the presence of QTM (Figure 7). Noteworthy, this magnetic blocking which is essentially the retention of a magnetic moment after removal of the external field, is unlikely

to occur for a dinuclear Dy^{III} complex containing a diamagnetic bridging ligand with nitrogen donor atoms.

To this end, a M vs. H curve was collected for **3** at 2 K between -7 and +7 T at a 100 Oe/s sweep rate. Excitingly, this measurement revealed the retention of magnetization upon removal of the external magnetic field giving rise to a coercive field H_c of 825 Oe at 2 K. With rising temperatures, the coercive fields decrease in value. The hysteresis loops remain open until 5 K, where H_c is smaller than the sweep rate. Noteworthy, the observation that hysteresis loops are open at such high temperatures is extremely rare for polynuclear lanthanide compounds where the metal ions are bridged by closed-shell ligands of the first row p -block elements.^{67–69} For example, comparable dinuclear benzotriazole/aminobipyrimidine or indigo (ind) bridged dysprosocenium complexes exhibit waist-constricted hysteresis loops at 1.8 K with no significant coercivity.^{67,68} Oftentimes, this is attributed to the presence of strong equatorial interaction of these ligands with the Dy^{III} f -electron density, which instils mixing of the m_j states and gives rise to effective QTM. Furthermore, the hysteresis curves for **3** exhibit steps, indicative of the presence of QTM at these temperatures. To probe whether the steps in the hysteresis loops and the relaxation observed in the ac magnetic susceptibility data collected at 6 K under varying field can be potentially correlated, the first derivative of the magnetization (dM/dH vs H) was investigated, where accelerations of the magnetic relaxation should become visible as signals (Fig. S29). At 2 K, three asymmetric, yet clearly discernible peaks at 1168, -1082 and -3513 Oe (scanning from +7 T towards -7 T) became apparent, alongside of two minima at 0 and -2407 Oe. The positions of the minima vary remain invariant traversing from negative to positive fields indicating that the first derivative is symmetric. As the temperatures were increased, the peaks gradually vanished, where the signal at ~ -3000 Oe decreases faster than the ones at $\sim \pm 1000$ Oe, until at 6 K these features are superimposed by noise.

Interestingly, although the variable-field magnetization data were collected at a different timescale relative to the ac data, the first signals coincide very well with the drop around 1000 Oe in the field-dependent AC measurements at 6 K (Fig. 6A). These peaks coincide with turning points of the hysteresis loops displayed in Fig. 7 and could be an indication for potential level crossings due to intramolecular coupling or hyperfine coupling. Given a small intramolecular zJ' was taken into account to fit the χ_{MT} vs T data for the Gd complex **2**, it can be hypothesised that these intermolecular effects are equally operative in the Dy^{III} congener and contribute to an increase of relaxation times. The effects of hyperfine coupling in various Dy isotopologues can be detrimental for the relaxation behaviour,⁷⁰ although the fields at which the steps in the hysteresis loops are largely invariant with different Dy^{III} isotopes. However, diamagnetic dilution of ¹⁶²Dy versus ¹⁶³Dy samples result in open magnetic hysteresis loops which without dilution show a butterfly-shaped hysteresis loop. Future studies will focus on deconvolution of these type of mechanisms.

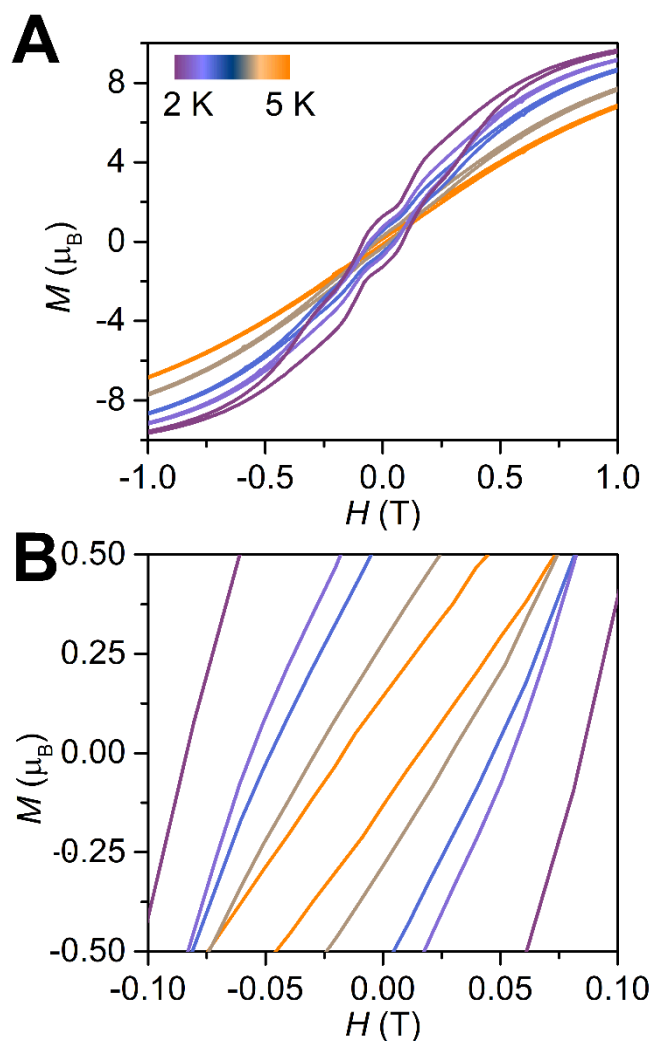


Figure 7. Isothermal variable-field magnetization (M) data collected for **3** collected between 2 and 5 K with an average sweep rate of 0.01 T s^{-1} (A). Magnification of the M vs. H curves for comparison, with a maximum coercive field H_c of 825 Oe (B).

In addition, isothermal magnetization curves were collected for **2** and **3** between 0 and 7 T at temperatures between 2 and 10 K (Figure S28). The curves for both complexes show gradual growth without inflection points signifying the lack of strong magnetic coupling and/or magnetic blocking. The saturation magnetization is reached for both samples at 2 K, plateauing at moments of $14.90 \mu_B$ (**2**) and $11.11 \mu_B$ (**3**), respectively. These moments are substantially lower than the expected values of $2 \times 7.94 \mu_B$ and $2 \times 10.65 \mu_B$ for two noninteracting Gd^{III} and Dy^{III} ions, respectively. However, the experimental values are close to the saturation magnetization values observed for other bridged didysprosocenium complexes^{44,71} e.g. $14.03 \mu_B$ (Gd) and $10.39 \mu_B$ (Dy) in $[(\text{Cp}^*_2\text{Ln})_2(\mu\text{-ind})]$.⁷¹ In fact, crystal field effects may engender a reduced magnetization since they remove the degeneracy of the spin ground states and induce splitting of the m_j states. Notably, these crystal field effects are reflected in the reduced magnetization plots (M vs. H/T), Figure S28. For **2**, these curves are essentially superimposed in accordance with weak crystal field effects on the m_j manifold, and the curves for **3** deviate significantly from ideal superposition, reflecting a considerable splitting among the m_j states. This also highlights

the presence of substantial magnetic anisotropy in **3**. Similar to the studies of the magnetic hysteresis loops, the first derivative of the magnetization data was scrutinized. At 2 K, the derivative exhibits a feature with two maxima at 676 and 2624 Oe, which disappears at 6 K (Fig. S30 and S31). This is in accord with the peaks observed in the derivative obtained from the hysteresis data (starting at 0 Oe applied field), but occur at much lower fields, possibly owing to differing measurement modes employed for both data sets and not of molecular origin. Such features in the derivative magnetization of other didysprosocene complexes containing diamagnetic bridges have been ascribed to metamagnetization-like behavior.⁷²

The strong magnetic anisotropy in **3** is also reflected in the orientation of the $m_j = \pm^{15}/2$ state of Dy^{III} as calculated by Magellan,²³ where the anisotropy is determined through the Cp* framework despite the presence of the equatorial dianionic bim ligand (Figure 2, assuming -0.5 charges residing on each bridging N atom and -0.2 on each central Cp* C atom).

Conclusions

The foregoing findings demonstrate that 2,2'-bisimidazole could be successfully employed in rare earth metal chemistry to generate a series of new organometallic compounds in good yields. In fact, the results on hand constitute the first utilization of the bisimidazole bridging ligand in the realm of lanthanide-containing single-molecule magnets. The Dy congener demonstrates zero-field dynamic magnetic properties with an effective energy barrier to spin reversal of $U_{\text{eff}} = 154(2) \text{ cm}^{-1}$ and remarkably, and open magnetic hysteresis loops below 5 K. Noteworthy, such magnetic memory is unusual for polynuclear dysprosium complexes with bridging, diamagnetic organic ligands. The strength of magnetic exchange coupling was quantified for the Gd congener, revealing weak antiferromagnetic coupling with $J = -0.074(2) \text{ cm}^{-1}$ (at 0.1 T). The similar trend for the $\chi_M T$ vs. T plot of **3** alludes to weak Dy^{III}-Dy^{III} coupling which is indicative of the SMM properties to be likely originating from single-ion anisotropy, rather than from a coupled state. The electronic structure of **1** was studied through DFT calculations and an in-depth comparison of the dianions bim²⁻ and the larger analogue Bbim²⁻ were carried out. This provided a profound insight into the redox inactivity of bim²⁻ relative to the redox activity of Bbim²⁻. Importantly, the calculated electron affinities confirm the experimentally observed redox inactivity of bim and the redox activity of Bbim. Hence, the annellation of the central bim moiety in **1-3** tunes the bridging ligand's electronic structure such that the population of a low-lying π^* becomes possible and therefore enables the isolation of the stable trianionic Bbim³⁻ radical. Thus, the electron affinity could serve as a theoretical tool to predict the redox activity of bridging entities. This discovery has huge ramifications moving forward in exploring new bridging ligands and assessing their reducibility. The foregoing results also pave the way for the construction of both higher nuclearity arrays innate to more than two paramagnetic lanthanide ions by utilizing the bim²⁻ ligand, and molecular qubits.

Conflicts of interest

There are no conflicts to declare.

Acknowledgements

S.D. is grateful to the Department of Chemistry at Michigan State University (MSU) for generous start-up funds. This work was supported in part through computational resources and services provided by the Institute for Cyber-Enabled Research, as well as the Max T. Rodgers NMR facility at MSU. Funding for the single-crystal X-ray diffractometer was provided through the MRI program of the National Science Foundation under Grant No. CHE-1919565.

Notes and references

- P. L. Arnold, M. W. McMullon, J. Rieb and F. E. Kühn, C-H bond Activation by *f*-block Complexes, *Angew. Chem. Int. Ed.*, 2015, **54**, 82–100.
- J. C. G. Bünzli and C. Piguet, Taking Advantage of Luminescent Lanthanide Ions, *Chem. Soc. Rev.*, 2005, **34**, 1048–1077.
- H. F. Li, P. F. Yan, P. Chen, Y. Wang, H. Xu and G. M. Li, Highly Luminescent Bis-Diketone Lanthanide Complexes with Triple-Stranded Dinuclear Structure, *Dalt. Trans.*, 2012, **41**, 900–907.
- A. P. Bassett, S. W. Magennis, P. B. Glover, D. J. Lewis, N. Spencer, S. Parsons, R. M. Williams, L. De Cola and Z. Pikramenou, Highly Luminescent, Triple- and Quadruple-Stranded, Dinuclear Eu, Nd, and Sm(III) Lanthanide Complexes Based on Bis-Diketonate Ligands, *J. Am. Chem. Soc.*, 2004, **126**, 9413–9424.
- R. Sessoli, D. Gatteschi, A. Caneschi and M. A. Novak, Magnetic Bistability in a Metal-Ion Cluster, *Nature*, 1993, **365**, 141–143.
- A. Caneschi, D. Gatteschi, R. Sessoli, A. L. Barra, L. C. Bruneir and M. Guillot, Alternating Current Susceptibility, High Field Magnetization, and Millimeter Band EPR evidence for a ground $S = 10$ state in $[\text{Mn}_{12}\text{O}_{12}(\text{CH}_3\text{COO})_{16}(\text{H}_2\text{O})_4] \cdot 2 \text{ CH}_3\text{COOH} \cdot 4 \text{ H}_2\text{O}$, *J. Am. Chem. Soc.*, 1991, **113**, 5873–5874.
- F. Guo, B. M. Day, Y. Chen, M. Tong, A. Mansikkamäki and R. A. Layfield, Magnetic Hysteresis up to 80 Kelvin in a Dysprosium Metallocene Single-Molecule Magnet, *Science*, 2018, **362**, 1400–1403.
- S. Demir, M. I. Gonzalez, L. E. Darago, W. J. Evans and J. R. Long, Giant Coercivity and High Magnetic Blocking Temperatures for N_2^{3-} Radical-Bridged Dilanthanide Complexes upon Ligand dissociation, *Nat. Commun.*, 2017, **8**, 2144.
- S. Demir, I. R. Jeon, J. R. Long and T. D. Harris, Radical ligand-containing single-molecule magnets, *Coord. Chem. Rev.*, 2015, **289–290**, 149–176.
- C. A. Gould, K. R. McClain, D. Reta, J. G. C. Kragoskow, D. A. Marchiori, E. Lachman, E. Choi, J. G. Analytis, R. D. Britt, N. F. Chilton, B. G. Harvey and J. R. Long, Ultrahard Magnetism from Mixed-Valence Dilanthanide Complexes with Metal–Metal Bonding, *Science*, 2021, **202**, 198–202.
- Z. Zhu and J. Tang, Metal-Metal Bond in Lanthanide Single-Molecule Magnets, *Chem. Soc. Rev.*, 2022, **51**, 9469–9481.
- Z. Zhu and J. Tang, Lanthanide Single-Molecule Magnets with High Anisotropy Barrier: Where to From Here?, *Natl. Sci. Rev.*, 2022, **9**, 5–7.
- H. Li, S. Wu and M. Tong, Lanthanide–Radical Single-Molecule Magnets: Current Status and Future Challenges, *Chem. Commun.*, 2023, DOI:10.1039/d2cc07042a.

- 14 A. Das, S. M. Mobin and G. K. Lahiri, Recognition of Fractional Non-Innocent Feature of Osmium Coordinated 2,2'-Biimidazole or 2,2'-Bis(4,5-dimethylimidazole) and Their Interactions with Anions., *Dalton Trans.*, 2015, **44**, 13204–13219.
- 15 Y. Li, X. R. Chang, X. J. Sang, J. S. Li, Y. H. Luo, Z. M. Zhu and W. S. You, Keggin-Type Polyoxometalate Modified Ag/Graphene Composite Materials for Electrocatalytic Water Oxidation, *Eur. J. Inorg. Chem.*, 2019, **31**, 3597–3604.
- 16 S. Fortin and A. L. Beauchamp, Preparations, Characterizations, and Structures of (Biimidazole)dihalobis(triphenylphosphine)Rhenium(iii) Salts: Strong Ion-Pairing and Acid - Base Properties, *Inorg. Chem.*, 2001, **40**, 105–112.
- 17 E. S. S. A, J. Calhorda and R. Dias, Di- η^5 -Cyclopentadienylmetal Complexes with Nitrogen Donor Atom Ligands: New Imidazole, *N*-Methylimidazole, Pyrazole and 2,2'-Bisimidazole Complexes of Molybdenum and Tungsten, *J. Organomet. Chem.*, **197**, 291-302.
- 18 G. S. Matouzenko, J. F. Létard, S. Lecocq, A. Bousseksou, L. Capes, L. Salmon, M. Perrin, O. Kahn and A. Collet, Two-step spin crossover in a mononuclear compound [Fe(DPEA)(bim)](ClO₄)₂·0.5 H₂O [DPEA = (2-aminoethyl)-bis(2-pyridylmethyl)amine, bim = 2,2'-bisimidazole] - Crystal Structure, Magnetic Properties, Mössbauer Spectroscopy, and Photomagnetic Effects, *Eur. J. Inorg. Chem.*, 2001, **11**, 2935–2945.
- 19 M. Tadokoro, K. Isogai, S. Harada, T. Kouchi, T. Yamane, T. Sugaya and H. Kamebuchi, Evidence of Poton-Coupled Mixed-Valency by Electrochemical Behavior on Transition Metal Complex Dimers Bridged by two Ag⁺ Ions, *Dalton Trans.*, 2019, **48**, 535–546.
- 20 Y. R. Zhong, M. L. Cao, H. J. Mo and B. H. Ye, Syntheses and Crystal Structures of Metal Complexes with 2,2'-biimidazole-like Ligand and Chloride: Investigation of X-H...Cl (X = N, O, and C) Hydrogen Bonding and Cl- π (imidazolyl) interactions, *Cryst. Growth Des.*, 2008, **8**, 2282–2290.
- 21 D. P. Rillema, R. Sahai, P. Matthews, A. K. Edwards, R. J. Shaver and L. Morgan, Multimetallic Ruthenium (II) Complexes Based on Biimidazole and Bibenzimidazole: Effect of Dianionic Bridging Ligands on Redox and Spectral Properties, *Inorg. Chem.*, 1990, **29**, 167–175.
- 22 P. Maślewski, K. Kazimierzczuk, Z. Hnatejko and A. Dołęga, Isostructural Zinc and Cadmium Silanethiolates with Bridging Biimidazole Co-Ligands – Enhanced Luminescence of Zinc Complex, *Inorg. Chim. Acta*, 2017, **459**, 22–28.
- 23 N. F. Chilton, D. Collison, E. J. L. McInnes, R. E. P. Winpenny and A. Soncini, An Electrostatic Model for the Determination of Magnetic Anisotropy in Dysprosium Complexes, *Nat. Commun.*, 2013, **4**, 2551.
- 24 R. P. Sharma, A. Singh, P. Brandão, V. Félix and P. Venugopalan, Syntheses, Characterization, Thermal Properties and Single Crystal Structure Determination of Cobalt(III) Complexes with 2,2'-Biimidazole and 1,10-Phenanthroline Ligands, *Polyhedron*, 2011, **30**, 2759–2767.
- 25 S. W. Kaiser, R. B. Saillant, W. M. Butler and P. G. Rasmussen, Rhodium and Iridium Complexes of Biimidazole. 1. Mononuclear and Dinuclear Species, *Inorg. Chem.*, 1976, **15**, 2681–2688.
- 26 B. F. Fieselmann, D. N. Hendrickson and G. D. Stucky, Synthesis, Electron Paramagnetic Resonance, and Magnetic Studies of Binuclear Bis(η^5 -Cyclopentadienyl)Titanium(III) Compounds with Bridging Pyrazolate, Biimidazolate, and Bibenzimidazolate Anions, *Inorg. Chem.*, 1978, **17**, 2078–2084.
- 27 K. K. Kamar, L. R. Falvello, P. E. Fanwick, J. Kim and S. Goswami, Designed Synthesis of a Multimetallic System Having Ru₄Cu₂ Core using Trimetallic Coordination of 2,2'-Biimidazolate Ion, *Dalton Trans.*, 2004, 1827–1831.
- 28 Y. H. Tan, J. S. Wu, C. S. Yang, Q. R. Liu, Y. Z. Tang, Y. R. Zhong and B. H. Ye, Spontaneous Resolution of Novel Zn Complexes in the Formation of 3d Metal-Organic Frameworks based on 2,2'-Biimidazole Ligand, *Inorg. Chim. Acta*, 2013, **399**, 45–49.
- 29 S. Y. Shi, L. Y. Chen, T. H. Zhu, J. Zhang and X. B. Cui, Two new Compounds of Polyoxoanions, Transition Metal Complexes and Organic Amines, *Inorg. Chim. Acta*, 2018, **477**, 292–299.
- 30 Z. Shi, J. Peng, X. Yu, Y. Shen, Z. Zhang, K. Alimaje and X. Wang, A new 3d Keggin-POM based Metal-Organic Framework of Cu and H₂Biim: Assembly and Properties of Fluorescence and Electrochemistry, *Inorg. Chem. Commun.*, 2013, **28**, 85–89.
- 31 J. C. Zhong, S. Z. Ge, F. Wan, Y. Q. Sun and Y. P. Chen, A Series of Luminescent Lanthanide-Organic Complexes Constructed from *in situ* generated Dithiobenzoic acid, *J. Inorg. Organomet. Polym. Mater.*, 2014, **24**, 633–643.
- 32 S. S. Pedro, P. Brandão, F. N. Shi, J. C. G. Tedesco and M. S. Reis, A new Metal Organic Framework constructed of Co(II) Ions six and seven-coordinated: Synthesis, Structure and Magnetism, *Polyhedron*, 2014, **81**, 210–215.
- 33 R. L. Sang and L. Xu, Unprecedented Infinite Lanthanide Hydroxide Ribbons [Ln₃(μ_3 -OH)₃]_n⁶ⁿ⁺ in a 3-D Metal-Organic Framework, *Chem. Commun.*, 2013, **49**, 8344–8346.
- 34 H. J. Zhang, R. Q. Fan, X. M. Wang, P. Wang, Y. L. Wang and Y. L. Yang, Preparation, Characterization, and Properties of PMMA-doped Polymer Film Materials: A Study on the Effect of Terbium Ions on Luminescence and Lifetime Enhancement, *Dalton Trans.*, 2015, **44**, 2871–2879.
- 35 L. X. You, L. X. Cui, B. B. Zhao, G. Xiong, F. Ding, B. Y. Ren, Z. L. Shi, I. Dragutan, V. Dragutan and Y. G. Sun, Tailoring the Structure, Ph Sensitivity and Catalytic Performance in Suzuki-Miyaura Cross-Couplings of Ln/Pd MOFs based on the 1,1'-di(*p*-Carboxybenzyl)-2,2'-diimidazole Linker, *Dalton Trans.*, 2018, **47**, 8755–8763.
- 36 V. Goudy, A. Jaoul, M. Cordier, C. Clavaguéra and G. Nocton, Tuning the Stability of Pd(IV) Intermediates using a Redox Non-Innocent Ligand Combined with an Organolanthanide Fragment, *J. Am. Chem. Soc.*, 2017, **139**, 10633–10636.
- 37 D. Wang, J. Moutet, M. Tricoire, M. Cordier and G. Nocton, Reactive Heterobimetallic Complex Combining Divalent Ytterbium and Dimethyl Nickel Fragments, *Inorganics*, 2019, **7**, 58.
- 38 S. Demir, J. M. Zadrozny, M. Nippe and J. R. Long, Exchange Coupling and Magnetic Blocking in Bipyrimidyl Radical-Bridged Dilanthanide Complexes, *J. Am. Chem. Soc.*, 2012, **134**, 18546–18549.
- 39 C. Chen, Z. B. Hu, H. Ruan, Y. Zhao, Y. Q. Zhang, G. Tan, Y. Song and X. Wang, Tuning the Single-Molecule Magnetism of Dysprosium Complexes by a Redox-Noninnocent Diborane Ligand, *Organometallics*, 2020, **39**, 4143–4148.
- 40 F. Benner and S. Demir, Isolation of the Elusive Bisbenzimidazole Bbim^{3-•} Radical Anion and its Employment in a Metal Complex, *Chem. Sci.*, 2022, **13**, 5818–5829.
- 41 K. Kotwica, I. Wielgus and A. Proń, Azaacenes Based Electroactive Materials: Preparation, Structure, Electrochemistry, Spectroscopy and Applications - A Critical Review, *Materials*, 2021, **14**, 5155.
- 42 M. R. MacDonald, J. W. Ziller and W. J. Evans, Coordination and Reductive Chemistry of Tetrakisphenylborate Complexes of Trivalent Rare-Earth Metallocene Cations, [(C₅Me₅)₂Ln][(μ-Ph)₂BPh₂], *Inorg. Chem.*, 2011, **50**, 4092–4106.
- 43 P. Hartman and H. K. Chan, Application of the Periodic Bond Chain (PBC) Theory and Attachment Energy Consideration to derive the Crystal Morphology of Hexamethylmelamine, *Pharm. Res.*, 1993, **10**, 1052–1058.

- 44 E. Castellanos, F. Benner and S. Demir, Taming salophen in Rare Earth Metallocene Chemistry, *Inorg. Chem. Front.*, 2022, **9**, 1325–1336.
- 45 W. J. Evans, J. R. Walensky, F. Furche, A. G. Dipasquale and A. L. Rheingold, Trigonal-Planar versus Pyramidal Geometries in the Tris(Ring) Heteroleptic Divalent Lanthanide Complexes (C₅Me₅)Ln(μ - η^6 : η^1 -Ph)₂BPh₂: Crystallographic and Density Functional Theory Analysis, *Organometallics*, 2009, **28**, 6073–6078.
- 46 W. J. Evans, The Importance of Questioning Scientific Assumptions: Some Lessons from *f*-Element Chemistry, *Inorg. Chem.*, 2007, **46**, 3435–3449.
- 47 S. Demir, J. M. Zadrozny and J. R. Long, Large Spin-Relaxation Barriers for the Low-Symmetry Organolanthanide Complexes [Cp*₂Ln(BPh₄)] (Cp* = Pentamethylcyclopentadienyl; Ln = Tb, Dy), *Chem. Eur. J.*, 2014, **20**, 9524–9529.
- 48 F. Neese, Software Update: The Orca Program System—Version 5.0, *Wiley Interdiscip. Rev. Comput. Mol. Sci.*, 2022, **12**, 1–15.
- 49 C. G. Zhan, J. A. Nichols and D. A. Dixon, Ionization Potential, Electron Affinity, Electronegativity, Hardness, and Electron Excitation Energy: Molecular Properties from Density Functional Theory Orbital Energies, *J. Phys. Chem. A*, 2003, **107**, 4184–4195.
- 50 J. Simons, Theoretical Study of Negative Molecular Ions, *Annu. Rev. Phys. Chem.*, 2011, **62**, 107–128.
- 51 C. P. Vibert and D. J. Tozer, Simple DFT Scheme for Estimating Negative Electron Affinities, *J. Chem. Theory Comput.*, 2019, **15**, 241–248.
- 52 N. F. Chilton, R. P. Anderson, L. D. Turner, A. Soncini and K. S. Murray, PHI: A Powerful New Program for the Analysis of Anisotropic Monomeric and Exchange-Coupled Polynuclear *d*- and *f*-Block Complexes, *J. Comput. Chem.*, 2013, **34**, 1164–1175.
- 53 P. Evans, D. Reta, C. A. P. Goodwin, F. Ortu, N. F. Chilton and D. P. Mills, A Double-Dysprosocenium Single-Molecule Magnet Bound together with Neutral Ligands, *Chem. Commun.*, 2020, **56**, 5677–5680.
- 54 D. Errulat, B. Gabidullin, A. Mansikkamäki and M. Murugesu, Two Heads are better than one: Improving Magnetic Relaxation in the Dysprosium Metallocene DyCp*₂BPh₄ upon Dimerization by Use of an Exceptionally Weakly-Coordinating Anion, *Chem. Commun.*, 2020, **56**, 5937–5940.
- 55 P. Zhang, F. Benner, N. F. Chilton and S. Demir, Organometallic Lanthanide Bismuth Cluster Single-Molecule Magnets, *Chem*, 2022, **8**, 717–730.
- 56 F. Tuna, C. A. Smith, M. Bodensteiner, L. Ungur, L. F. Chibotaru, E. J. L. McInnes, R. E. P. Winpenny, D. Collison and R. A. Layfield, A High Anisotropy Barrier in a Sulfur-Bridged Organodysprosium Single-Molecule Magnet, *Angew. Chem. Int. Ed.*, 2012, **51**, 6976–6980.
- 57 T. Pugh, A. Kerridge and R. A. Layfield, Yttrium Complexes of Arsine, Arsenide, and Arsinidene Ligands, *Angew. Chem. Int. Ed.*, 2015, **54**, 4255–4258.
- 58 T. Pugh, V. Vieru, L. F. Chibotaru and R. A. Layfield, Magneto-Structural Correlations in Arsenic- and Selenium-Ligated Dysprosium Single-Molecule Magnets, *Chem. Sci.*, 2016, **7**, 2128–2137.
- 59 T. Pugh, F. Tuna, L. Ungur, D. Collison, E. J. L. McInnes, L. F. Chibotaru and R. A. Layfield, Influencing the Properties of Dysprosium Single-Molecule Magnets with Phosphorus Donor Ligands, *Nat. Commun.*, 2015, **6**, 7492.
- 60 F. S. Guo, B. M. Day, Y. C. Chen, M. L. Tong, A. Mansikkamäki and R. A. Layfield, A Dysprosium Metallocene Single-Molecule Magnet Functioning at the Axial Limit, *Angew. Chem. Int. Ed.*, 2017, **56**, 11445–11449.
- 61 C. A. P. Goodwin, F. Ortu, D. Reta, N. F. Chilton and D. P. Mills, Molecular Magnetic Hysteresis at 60 Kelvin in Dysprosocenium, *Nature*, 2017, **548**, 439–442.
- 62 J. C. Vanjak, B. O. Wilkins, V. Vieru, N. S. Bhuvanesh, J. H. Reibenspies, C. D. Martin, L. F. Chibotaru and M. Nippe, A High-Performance Single-Molecule Magnet utilizing Dianionic Aminoborolide Ligands, *J. Am. Chem. Soc.*, 2022, **144**, 17743–17747.
- 63 A. H. Vincent, Y. L. Whyatt, N. F. Chilton and J. R. Long, Strong Axiality in a Dysprosium(III) Bis(borolide) Complex leads to Magnetic Blocking at 65 K, *J. Am. Chem. Soc.*, 2023, **145**, 1572–1579.
- 64 D. Reta and N. F. Chilton, Uncertainty Estimates for Magnetic Relaxation Times and Magnetic Relaxation Parameters, *Phys. Chem. Chem. Phys.*, 2019, **21**, 23567–23575.
- 65 H. L. C. Feltham and S. Brooker, Review of Purely 4*f* and Mixed-Metal *nd-4f* Single-Molecule Magnets containing only one Lanthanide Ion, *Coord. Chem. Rev.*, 2014, **276**, 1–33.
- 66 D. Aravena and E. Ruiz, Spin Dynamics in Single-Molecule Magnets and Molecular Qubits, *Dalton Trans.*, 2020, **49**, 9916–9928.
- 67 R. A. Layfield, J. J. W. McDouall, S. A. Sulway, F. Tuna, D. Collison and R. E. P. Winpenny, Influence of the *N*-Bridging Ligand on Magnetic Relaxation in an Organometallic Dysprosium Single-Molecule Magnet, *Chem. Eur. J.*, 2010, **16**, 4442–4446.
- 68 J. O. Moilanen, A. Mansikkamäki, M. Lahtinen, F. S. Guo, E. Kalenius, R. A. Layfield and L. F. Chibotaru, Thermal Expansion and Magnetic Properties of Benzoquinone-Bridged Dinuclear Rare-Earth Complexes, *Dalton Trans.*, 2017, **46**, 13582–13589.
- 69 P. Zhang, M. Perfetti, M. Kern, P. P. Hallmen, L. Ungur, S. Lenz, M. R. Ringenberg, W. Frey, H. Stoll, G. Rauhut and J. van Slageren, Exchange Coupling and Single Molecule Magnetism in Redox-Active Tetraoxolene-Bridged Dilanthanide Complexes, *Chem. Sci.*, 2018, **9**, 1221–1230.
- 70 J. Flores Gonzalez, F. Pointillart and O. Cador, Hyperfine coupling and Slow Magnetic Relaxation in Isotopically Enriched Dy^{III} Mononuclear Single-Molecule Magnets, *Inorg. Chem. Front.*, 2019, **6**, 1081–1086.
- 71 F.-S. Guo and R. A. Layfield, Strong Direct Exchange Coupling and Single-Molecule Magnetism in Indigo-Bridged Lanthanide Dimers, *Chem. Commun.*, 2017, **53**, 3130–3133.
- 72 Y. S. Meng, J. Xiong, M. W. Yang, Y. Sen Qiao, Z. Q. Zhong, H. L. Sun, J. B. Han, T. Liu, B. W. Wang and S. Gao, Experimental Determination of Magnetic Anisotropy in Exchange-Bias Dysprosium Metallocene Single-Molecule Magnets, *Angew. Chem. Int. Ed.*, 2020, **59**, 13037–13043.